Two-dimensional modeling of high plasma density inductively coupled sources for materials processing

Peter L. G. Ventzek, Robert J. Hoekstra, and Mark J. Kushner[a)]
Department of Electrical and Computer Engineering, University of Illinois, Urbana, Illinois 61801

(Received 26 August 1993; accepted 21 September 1993)

Inductively coupled plasma sources are being developed to address the need for high plasma density (10^{11}–10^{12} cm^{-3}), low pressure (a few to 10–20 mTorr) etching of semiconductor materials. One such device uses a flat spiral coil of rectangular cross section to generate radio-frequency (rf) electric fields in a cylindrical plasma chamber, and capacitive rf biasing on the substrate to independently control ion energies incident on the wafer. To investigate these devices we have developed a two-dimensional hybrid model consisting of electromagnetic, electron Monte Carlo, and hydrodynamic modules; and an off line plasma chemistry Monte Carlo simulation. The results from the model for plasma densities, plasma potentials, and ion fluxes for Ar, O_2, Ar/CF_4/O_2 gas mixtures will be presented.

I. INTRODUCTION

The trend in plasma processing, and plasma etching in particular, is towards reactors using lower pressure (<a few to 10s mTorr) and discharges which operate with a low and controllable bias on the substrate.[1–3] These systems have the potential of generating fewer particles. They also have less ion scattering which may result in a more anisotropic flux to the wafer, and produce lower energy ions which may produce a less damage to the wafer. Since the rate of radical generation of proportional to $k[e][N]$ (k is the electron impact rate coefficient, $[e]$ the electron density and $[N]$ is the gas density), lower pressure etching systems must operate at higher plasma densities to achieve the same processing rate as conventional high pressure (10s–100s mTorr) reactive ion etching (RIE) systems.

In this regard, electron cyclotron resonance (ECR) discharges have received considerable attention in recent years for high plasma density, low pressure etching, and deposition applications.[1,4,5] Plasma densities of 10^{11}–10^{12} cm^{-3} can be achieved in ECR reactors with input microwave powers of 100s W to 1–2 kW. Although promising etching performances have been obtained with ECR reactors, there are a few inherent difficulties in scaling them to larger wafer sizes (>200 mm). For example, obtaining ECR excitation in conventional reactors (2.45 GHz) requires generating magnetic fields of 875 G over a large cross-sectional area. This results in slightly magnetized ions, which follow the divergent magnetic field lines to the wafer, thereby compromising uniformity. Magnetized electrons in ECR discharges can be accelerated to energies >100s eV resulting in x-ray production, which is potentially damaging to the product.[6] Distributed ECR sources may avoid many of these problems.[1] In spite of the promise of ECR systems, issues related to cost of ownership and scalability have motivated development of alternate low pressure plasma sources.

Inductively coupled plasmas (ICPs) in the form of barrel reactors were among the first discharges used for the etching of semiconductors.[7] They were nearly abandoned by the semiconductor processing community for other than cleaning purposes due to their inability to etch fine anisotropic features. Recently, though, new ICP configurations have been introduced by workers at IBM East Fishkill and LAM Research Inc. which are capable of producing high density (10^{11}–10^{12} cm^{-3}) plasmas at low pressure (<10–20 mTorr), while uniformly etching anisotropic features over large wafers.[8–11] Similar reactor configurations have also been investigated by Hopwood[2,12–14] and Wendt.[15]

A schematic of a typical ICP reactor is shown in Fig. 1. The reactor is a squat cylinder with a dielectric roof. The roof-to-substrate height is 5–15 cm. The plasma zone is 10–30 cm in diameter, chosen to accommodate wafers of the desired size. The plasma is generated by an inductively coupled azimuthal electric field produced by a flat antenna. The antenna is generally a spiral coil of rectangular cross-section placed on the top of the dielectric roof. Applied voltage to the antenna at 13.56 MHz generates an oscillating magnetic field around the coil, which penetrates into the plasma and produces an azimuthal electric field schematically shown in Fig. 1. In an ideal reactor, the azimuthal electric field E_θ, is zero on the axis and zero on the periphery, thereby peaking in an annular region at roughly half the radius. In carefully designed reactors, the fractional amount of power capacitively coupled into the plasma from the coil can be small, thereby generating a quiescent plasma potential which does not significantly oscillate during the radio-frequency (rf) cycle. However, to control the ion energies incident on the wafer, the substrate can be optionally biased by independently applying a rf potential. Optional multipole magnets can also be placed on the outer periphery of the chamber to produce a magnetic bucket. The effect of the magnetic bucket is to smooth the plasma density in the radial direction, reduce the plasma potential, and ultimately increase the plasma density for a given power deposition.[2,12] Plasma densities of 10^{11}–10^{12} cm^{-3} have been measured in Ar and O_2 at gas pressures of 2–20 mTorr for power depositions of 100s W–1 kW in a 20 cm (diameter) ×7.5 cm (height) chamber. The plasma potentials for these conditions are 10–30 V.[8–11]

To investigate plasma generation mechanisms and plasma

[a)]Author to whom correspondence should be addressed.

 0734-211X/94/12(1)/461/17/$1.00 ©1994 American Vacuum Society

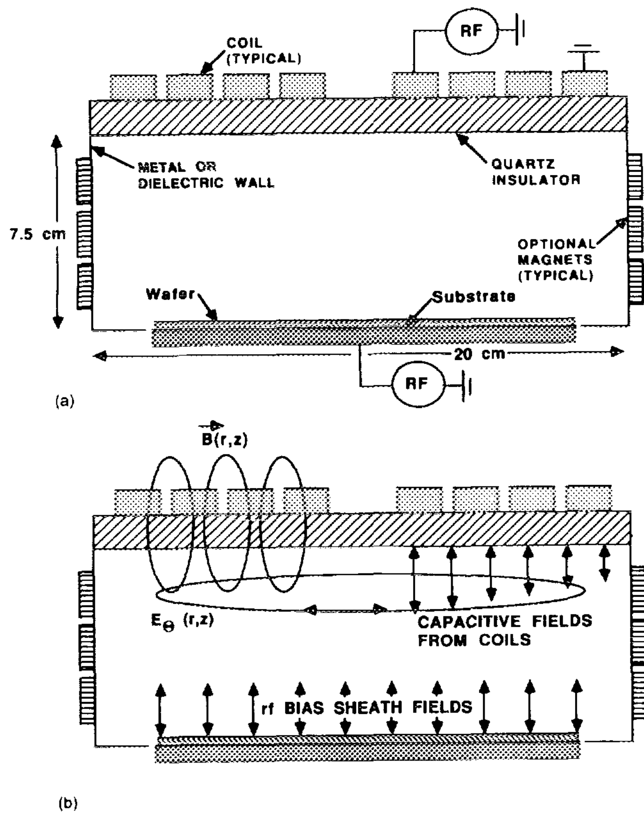

FIG. 1. Schematics of the inductively coupled plasma source. (a) The rectangular cross section coil is driven at 13.56 MHz and placed on a dielectric roof. Optional cusp field magnets form a magnetic bucket. The substrate is also optionally rf biased. (b) The coil produces magnetic fields $\mathbf{B}(r,z)$ which generate an azimuthal electric field $E_\theta(r,z)$. Additional electric fields are generated by the applied capacitive rf bias on the substrate and by capactive coupling from the coil.

transport in ICP reactors, a computer model has been developed using the geometry shown in Fig. 1.[16,17] The model is a hybrid simulation which combines an electromagnetic module, an electron Monte Carlo simulation, and a hydrodynamic simulation to obtain species densities and fluxes as a function of position (r, z). Ion energy distributions to the substrate are obtained from a companion plasma chemistry Monte Carlo simulation. The model will be described in Sec. II followed by a discussion of results from the model and comparison to experiment in Sec. III. Our concluding remarks are in Sec. IV.

II. DESCRIPTION OF THE MODEL

Two-dimensional (2D) models of capacitively coupled plasma processing reactors have recently been published using fluid[18-20] and particle techniques.[21] Our model for ICP reactors is a hybrid simulation consisting of an electromagnetic module (EMM), an electron Monte Carlo simulation (EMCS), a fluid-chemical kinetics simulation (FKS), and an off-line plasma chemistry Monte Carlo simulation (PCMCS). A schematic of the model is shown in Fig. 2. The model uses a 2D cylindrically symmetric (r,z) geometry. The simulation begins by calculating the coil generated electric and magnetic fields $E(r,z,\phi)$ and $B(r,z,\phi)$ as a function of position

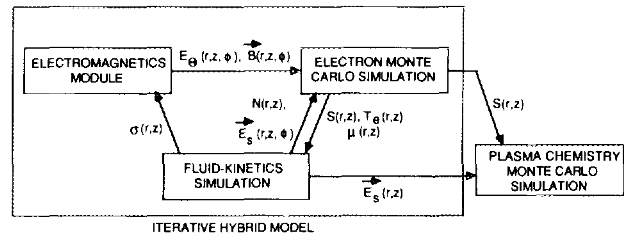

FIG. 2. Schematic of the hybrid model for ICP discharges. The EMM generates magnetic $[\mathbf{B}(r,z,\phi)]$ and electric fields $[E_\theta(r,z,\phi)]$ produced by the coil for use in an EMCS. The EMCS produces source functions and transport coefficients for the FKS. The FKS produces electrostatic electric fields $[E_s(r,z,\phi)]$ and species densities for use in the EMCS, and the conductivity $[\sigma(r,z)]$ for use in the EMM. The sequence is iterated until plasma densities converge. Source functions and electric fields are then exported to an off-line plasma chemistry Monte Carlo simulation.

and phase during the rf cycle using the EMM. To initially obtain these fields, we estimate the plasma conductivity $\sigma(r,z)$. These fields are then used in the EMCS for electron trajectories. In the EMCS, the time averaged electron energy distribution, $f(\epsilon,r,z)$, is obtained by advancing and recording electron trajectories over ≈ 50 rf cycles using the fields from the EMM. During the first iteration of the model, electrostatic fields $E_s(r,z,\phi)$ are estimated. $f(\epsilon,r,z)$ is then used to calculate source functions for electron impact processes, $S_j(r,z)$, diffusion coefficients $D(r,z)$, mobilities $\mu(r,z)$, and average electron temperatures $T_e(r,z)$.

The source functions and transport coefficients are then used in the FKS, which solves for the densities of all charged and neutral species and for the electrostatic plasma potential. The FKS is integrated for 10s–100s of rf cycles. The time averaged conductivities are then transferred to the EMM. $E_s(r,z,\phi)$ and time averaged species densities are transferred to the EMCS. The modules are sequentially iterated, beginning with the EMM, until the cycle averaged plasma densities in the FKS converge.

After the model converges, the source functions ($cm^{-3}s^{-1}$) of ions and radicals generated in the EMCS and and $E_s(r,z)$ produced in the FKS are used in a separate plasma chemistry Monte Carlo simulation. In the PCMCS, the trajectories of ions and radicals are followed throughout the reactor, while accounting for elastic and charge exchange collisions as well as chemical reactions. The end result is the ion flux and ion energy distributions as a function of position on the wafer. Each of the submodels will now be described.

A. Electromagnetic module (EMM)

The electromagnetic module solves for $E(r,z,\phi)$ and $B(r,z,\phi)$. The method of solution is functionally the same as used by Yu and Girshick.[22] The electric field is obtained by solving the complex wave equation

$$\nabla^2 E_\theta(r,z) = i\omega\mu_0\sigma(r,z)E_\theta(r,z), \tag{1}$$

where we assume a purely sinusoidal field driven at frequency ω (rad/s) and $E_\theta(r,z)$ is the complex amplitude of the azimuthal component of the electric field. The amplitude is obtained by solving Eq. (1) within the volume of the plasma using the method of successive-over-relaxation

(SOR) in cylindrical coordinates. The boundary conditions are $E_\theta(r=0,z)=E_\theta(r=R,z)=E_\theta(r,z=0)=0$; where the radius of the chamber is R and $z=0$ is the substrate. These boundary conditions are obtained by assuming that the field is purely azimuthal, and that the walls of the chamber and the wafer holder are metallic. The boundary condition at the top surface of the plasma (below the dielectric roof), $E_\theta(r,z=H)$, is obtained in the following fashion.

The coils are divided into individual current loops. The total current is distributed through the cross section of the coils by specifying a skin depth in the metal. Although the coil is typically a spiral, we only resolve a cross section of the coil; and so the coil appears as nested annuli. The electric fields due to the coil currents and due to the plasma currents are summed to provide $E_\theta(r,z=H)$. This field can be analytically obtained from[22]

$$E_\theta(r,z=h)=\frac{\omega\mu_0}{2\pi}\left[-i\sum_l I_l\left(\frac{r_l}{r}\right)^{1/2}G(k_l)+\sum_{m,n} j_{m,n}A_{m,n}\times\left(\frac{r_{m,n}}{r}\right)^{1/2}G(k_{m,n})\right], \tag{2a}$$

$$G(k_l)=\frac{(2-k_l^2)\mathcal{K}(k_l)-2\mathcal{E}(k_l)}{k_l}, \tag{2b}$$

$$k_l=2\left(\frac{r_l r}{(r_l+r)^2+(H-z_l)^2}\right)^{1/2}, \tag{2c}$$

$$j_{m,n}=\sigma_{m,n}E_{m,n}. \tag{2d}$$

In Eq. (2a), the first sum is over the individual current loops l in the coil having current I_l and radius r_l. The second sum is over current sources in the plasma at (r,z) location m,n having current density $j_{m,n}$, conductivity $\sigma_{m,n}$, and cross-sectional area $A_{m,n}$. $\mathcal{K}$ and $\mathcal{E}$ are the incomplete elliptic integrals of the first and second kinds. The second sum models the plasma as a superposition of current loops.

To start the EMM, the coil current is specified. $E_\theta(r,z=h)$ is then generated using these coil currents and plasma currents obtained from $\sigma(r,z)E_\theta(r,z)$ with the field being estimated from the vacuum configuration. The SOR is then executed to update $E_\theta(r,z)$. When $E_\theta(r,z)$ has converged, it is then used in Eq. (2) to update the boundary condition $E_\theta(r,z=H)$. The process is repeated until the solution converges. This procedure is quite sensitive to the value of the SOR parameter at high conductivities [$\sigma>0.1$ $(\Omega\ \mathrm{cm})^{-1}$]. The SOR parameter α is the quantity which determines how much the iterative solution for E_θ is over relaxed and therefore determines the stability of the solution. A value of $\alpha=1$ reduces the SOR method to Gauss–Seidel iteration. Typically we require SOR parameters of $1.2\leq\alpha\leq1.3$ to assure that the solution converges.

The parameter of interest is usually power deposition. In practice we obtain the solution described above with an arbitrary coil current. The coil current is proportional to the square root of the power deposition for a given $\sigma(r,z)$, and $E_\theta(r,z)$ is linearly proportional to the coil current. At the end of the EMM, the coil current and $E_\theta(r,z)$ are rescaled to yield the specified power deposition. The relative phase of $E(r,z,\phi)$ is obtained from the complex components of $E_\theta(r,z)$. The r and z components of the magnetic field are then obtained from the converged $E_\theta(r,z)$ by $\mathbf{B}(r,z)=(i/\omega)\nabla\times\mathbf{E}$.

B. Electron Monte Carlo simulation (EMCS)

The EMCS is a 2D (r,z) model which follows electron trajectories using the electric $E(r,z,\phi)$ and magnetic $B(r,z,\phi)$ fields generated in the EMM and electrostatic fields $E_s(r,z,\phi)$ generated in the FKS. The mechanics of the EMCS are basically the same as the Monte Carlo model described in Ref. 23, and therefore will be only briefly discussed here.

Prior to beginning the simulation, the energy range of interest is discretized into bins centered on energies ϵ_i. Probability arrays for electron collisions with the gas atoms and molecules as a function of energy are constructed for all pertinent processes (e.g., elastic, excitation, ionization). The probability arrays are constructed from the collision frequencies

$$\nu_{ij}=\left(\frac{2\epsilon_i}{m_e}\right)^{1/2}\sigma_{ij}N_j, \tag{3}$$

where σ_{ij} is the electron impact cross section at energy i for process j, and N_j is the density of the collision partner for process j. The probability arrays are

$$P_{ij}=\left[\sum_{l=1}^{j}\nu_{il}+(\nu_m-\nu_i)\right]/\nu_m, \tag{4}$$

where

$$\nu_i=\sum_{l=1}^{l_{\max}}\nu_{il} \tag{5}$$

is the maximum collision frequency for energy i and $\nu_m=\max(\nu_i)$ is the maximum collision frequency for all energies. The probability arrays incorporate a null collision frequency $(\nu_m-\nu_i)$.

Electron trajectories and positions are initialized as being randomly selected from a Maxwellian and uniformly distributed in the reactor. The electron trajectories are advanced using second order integration with accelerations interpolated as a function of position and phase from the $E(r,z,\phi)$ and $B(r,z,\phi)$ obtained from the EMM. A time-varying electrostatic field $E_s(r,z,\phi)$ is also included, obtained from the FKS on successive iterations. Note that in the absence of capacitive coupling from the antenna, there is no *a priori* relationship between the phase of the inductive fields from the EMM and the phase of the electrostatic field from the FKS, as determined by an applied rf bias to the substrate.

When using a magnetic bucket, static magnetic cusp fields $B_c(r,z)$ are specified as input. Experimentally, the cusps are oriented in the azimuthal direction. Since we do not resolve this dimension, we orient the cusps in the axial direction. The spatial dependence of the cusps is

$$B_c(r,z)=B_0\ \mathrm{abs}\left[\cos\left(\frac{\pi x}{L}\right)^m\right]\exp\left[-\left(\frac{(R-r)}{\lambda}\right)^2\right], \tag{6}$$

where λ is the radial penetration distance, L is the axial period of the cusp, and m is a shape factor. The shape factor is chosen to approximate the same loss cone as the experimental azimuthally oriented cusps. For the magnetic bucket cases investigated here, we used $B_0=1.5$ kG, $\lambda=0.5$ cm, and $L=2.5$ cm.

Electron trajectories of each pseudoparticle are separately advanced using second-order integration with individual timesteps. The time steps for pseudoparticle l are

$$\Delta t_l=\min\left(0.01\,\tau_{\rm rf},\ 0.01\,\tau_{\rm ECR},\ t_{\rm cl}-t_l,\ \frac{\Delta t_{rz}}{4}\right), \tag{7}$$

where t_l is the time for particle l prior to updating the trajectory, $\tau_{\rm rf}$ is the radio frequency period, $\tau_{\rm ECR}$ is the local electron cyclotron period, $t_{\rm cl}$ is the time of the next collision, and Δt_{rz} is the time required to cross the local computational cell. Statistics are collected on the pseudoparticle's position, energy and phase following every advance of each particle after a sufficient number of rf cycles have been calculated to achieve a quasisteady state.

The time of the next collision is

$$t_{\rm cl}=t_{l0}+\nu_m^{-1}\ \ln(r), \tag{8}$$

where t_{l0} is the time of the last collision of pseudoparticle l and r is a random number (0,1). When $t_l \geq t_{\rm cl}$, a collision occurs. The particular collision is obtained by choosing another random number. The type of collision which occurs is that process which satisfies

$$P_{ij}<r<P_{i,j+1}. \tag{9}$$

Null collisions and scattering of the pseudoparticles are handled in the fashion described in Refs. 23 and 24. The probability arrays are updated on each iteration through the hybrid model using species densities (feedstock, excited state, radical, and ion) calculated in the previous iteration in the FKS.

The EMCS is performed for $\approx$20–50 rf cycles for each iteration through the hybrid model. At the conclusion of the EMCS, electron impact source functions for each process are calculated from the time averaged electron energy distribution $f(\epsilon,r,z)$ for use in the FKS.

The source function of process j for species i is

$$S_{ij}(r,z)=n_e(r,z)\,\delta_{ij}N_{ij}(r,z)\int_0^\infty f(\epsilon,r,z)\times\left(\frac{2\epsilon}{m_e}\right)^{1/2}\sigma_{ij}(\epsilon)d\epsilon, \tag{10}$$

where $n_e(r,z)$ and $N_{ij}(r,z)$ are the electron density and collision partner for the process ij obtained from the previous iteration of the FKS. δ_{ij} is ± 1 depending on whether process (ij) is a source or loss of species j. During the first few iterations through the hybrid these sources are computed each iteration. To aid with convergence on later iterations, the sources are back averaged with the previous iteration. The back averaging process is

$$S_k'=(1-\beta)S_k+\beta S_{k-1}', \tag{11}$$

where S_k' is the source function transferred to the FKS on the kth iteration, S_k is the source function computed in Eq. (10) for the current iteration, and β is the back averaging coefficient. We typically begin back averaging after the third or fourth iteration with $\beta=0.4$.

C. Fluid-chemical kinetics simulation (FKS)

Prior to beginning the FKS, we have generated a set of electron impact source functions and transport coefficients as a function of position. In the FKS, the continuity equations for all charged and neutral species, and Poisson's equation are solved

$$\frac{\partial N_j}{\partial t}=\nabla(\mu_j q_j N_j \mathbf{E}_s - D_j \nabla N_j)+\left(\frac{\partial N_j}{\partial t}\right)_c, \tag{12}$$

$$\nabla\cdot\mathbf{E}_s=-\nabla^2\Phi=\frac{\rho}{\epsilon_0}, \tag{13}$$

where μ_j is the mobility of species j, D_j is the diffusion coefficient, q_j is the species charge in units of the elementary charge, ρ is the charge density, $(\partial N_j/\partial t)_c$ is the change in density due to all collisions, E_s is the electrostatic field, and Φ is the electrostatic potential. $(\partial N_j/\partial t)_c$ contains contributions from both heavy particle collisions as well as the electron impact source functions, $S_j(r,z)$. Unless noted otherwise, the electron impact processes and heavy particle collisions are the same as in Refs. 23 and 25; and the same electron impact cross sections were used.

Since the gas pressure is low and Knudsen number large (Kn=0.1) conventional drift-diffusion equations may not well represent particle transport. We correct for low pressure effects by limiting the diffusion coefficient to be

$$D_j'=\min(v_{\rm th}\Lambda,D_j), \tag{14}$$

where $v_{\rm th}$ is the thermal speed of the species and Λ is the diffusion length of the reactor. This prevents the unphysical situation of species diffusing at a speed faster than $v_{\rm th}$. To ensure that the ambipolar fields are well represented, we must then rescale the particle mobility to satisfy the Einstein relation,

$$\mu_j=\frac{eD_j'}{kT_j}. \tag{15}$$

When using a magnetic bucket, the diffusion coefficients of all charged species are resolved into components parallel and perpendicular to the local magnetic field. $D_\parallel=D'$, whereas

$$D_\perp=\frac{D'}{1+(\omega_c/\nu_c)^2}, \tag{16}$$

where ω_c is the local ion or electron cyclotron frequency and ν_c is the local collision frequency. The multipole magnets in an ICP reactor are usually arranged so that the magnetic field varies in the azimuthal direction. Since our simulation does not resolve this dimension [our dimensions are (r,z)], we turned the multipole magnets in our model by 90° so that the variation in the magnetic field is in the axial direction, as described by Eq. (6).

In conventional plasma dynamics simulations, Poisson's equation for the electric potential and the charge continuity equation are separately solved. In explicit solutions of the transport equations, the time step is then constrained by the Courant limit,

$$\Delta t_c \leq \min\left(\frac{\Delta r}{\mu_j E_r}, \frac{\Delta z}{\mu_j E_z}\right), \tag{17}$$

where $(\Delta r, \Delta z)$ is the spatial mesh size, μ_j is the mobility of species j, and E is local electric field. In implicit solutions of the transport equations, the time step may exceed Δt_c. Conventional solutions of Poisson's equations are usually explicit regardless of the implicit or explicit nature of the solution for the charge densities. This can be seen by noting that the potentials Φ obtained for use in the update of the charge densities ρ from time t to time $t+\Delta t$ are obtained from present values of $\rho(t)$. In principle, this explicitness can be seen by writing

$$\nabla^2\Phi(t+\Delta t) = -\frac{\rho(t)}{\epsilon_o}. \tag{18}$$

In order for the electric field not to change sign during one time step, the maximum allowable time step between updates of the electrical potential (and hence the time step for the transport equations) is the dielectric relaxation time Δt_d given by[26]

$$\Delta t_d = \frac{\epsilon_0}{\sigma}, \tag{19}$$

where σ is the plasma conductivity. For the high-density low pressure discharges of interest, $\sigma \approx 0.1-1$ $(\Omega\ \mathrm{cm})^{-1}$, which results in $\Delta t_d \approx 10^{-13}-10^{-12}$ s. This value is typically orders of magnitude smaller than the Courant limit.

To overcome the limitation imposed by Δt_d, a semi-implicit update technique for the electric potential has been devised. In this scheme, the Poisson's equation is solved for a future time using a prediction for the charge densities based on the present values of their time derivatives:

$$\nabla^2\Phi(t+\Delta t) = -\frac{1}{\epsilon_0}\left[\rho(t) + \Delta t \frac{d\rho}{dt}(t)\right]. \tag{20}$$

Since the collisional portions of the continuity equations are conservative with respect to charge density at any given location, the time derviative for the charge density in Eq. (20) contains only transport terms:

$$\frac{d\rho}{dt} = \sum_i eq_i[\nabla(D\nabla N_i + q_i N_i \mu_i \nabla\Phi)], \tag{21}$$

where the sum is over all charged species. Writing Poisson's equation in this way effectively reforms the Laplacian operator since the drift terms on the right-hand side of Eq. (21) operate on the potentials. This can be seen by rewriting Eq. (21) as

$$\nabla^2\Phi(t+\Delta t) + \frac{1}{\epsilon_0}\Delta t \sum_i eq_i\mu_i[\nabla N_i \nabla\Phi(t+\Delta t) + N_i\nabla^2\Phi(t+\Delta t)] = -\frac{\rho(t)}{\epsilon_0} - \frac{1}{\epsilon_0}\Delta t e \sum_i q_i(\nabla D_i \nabla N_i). \tag{22}$$

This formulation is essentially Lagrangian since the effect of the added terms on the left-hand side of Eq. (22) is to distort the computational mesh to eliminate any change in charge density due to drift. Equation (22) is solved using the method of SOR using a convergence criterion of 0.01 V. The SOR parameter α was optimized for this application, and is in the range $1.8 \leq \alpha \leq 1.9$.

This semi-implicit algorithm allows the time steps to exceed Δt_d by factors of 100–1000, or until limited by the Courant criterion or a specified fraction of the rf cycle. Extensive tests were conducted in choosing time steps $\Delta t_d \leq \Delta t \leq \Delta t_c$ to validate the algorithm. In all cases, the potentials and densities obtained were identical to within a few tenths of a percent.

Boundary conditions for Poisson's equation depend on whether the surface is metallic of dielectric. If the surface is metallic, then the boundary value of the potential is specified by the surface being grounded or driven to a known potential. If the boundary is a dielectric, the potential on the surface of the dielectric in contact with the plasma Φ_0 is given by

$$\Phi_0 = \frac{\Phi_i + \Delta z[\sigma_s/\epsilon_0 + \epsilon_d\Phi_b/(\epsilon_0 L)]}{1 + \Delta z \epsilon_d/(L\epsilon_0)}. \tag{23}$$

In Eq. (23), Φ_1 is the plasma potential a distance Δz from the surface of the dielectric, ϵ_d is the permittivity of the dielectric, L is the thickness of the dielectric, Φ_b is the potential on the opposite side of the dielectric from the plasma, and σ_s is the surface charge density. The surface charge density (C cm^{-2}) is obtained by integrating the fluxes of all charged species to the surface

$$\sigma_s = \sum_j \int eq_j\phi_j\, dt, \tag{24}$$

where $\phi_j = (q_j\mu_j N_j \mathbf{E}_s - D_j\nabla N_j)\cdot\hat{n}$ is the flux to the surface. The local normal unit vector is $\hat{n}$. If the dielectric is bounded by a metal, as in the case of a wafer on a metallic substrate, Φ_b is simply the substrate potential or potential on the "far side" of the dielectric. For example, in RIE discharges a common configuration is to use a dielectric ring which separates the two electrodes axially, and is the boundary between the plasma and air in the radial direction. In this case Φ_b on the side of the dielectric open to air is uniformly graded between the potential of the two electrodes.

The speed with which the FKS converges to the steady state depends on the "goodness" of the initial guess of species number densities. We have found that 10s–100s μs are required for the solution to converge, which puts a large

premium on good initial guesses. For this reason, the FKS employs an acceleration scheme to improve the goodness of the initial guess of species densities.[21,27]

During a given iteration, the FKS is initially run in intervals of ≈ 100 ns or a fixed number of rf cycles. At the end of each interval, the plasma averaged time rate of change of density $(dN_j/dt)'$ is calculated for each species. The densities of all species (charged and neutral) are then accelerated for a time Δt_A, which is on the order of $1000-2000\Delta t$;

$$N_j(r,z,t+\Delta t_A)=N_j(r,z,t)+\gamma\left(\frac{dN_i}{dt}\right)'\Delta t_A. \quad (25)$$

γ is a factor which represents an algorithm which allows positive accelerations to proceed at a higher rate than negative accelerations. This algorithm is used to prevent the unphysical situation of driving charge densities to negative values and with the knowledge that many species slowly evolve from small to large densities. The acceleration typically yields an effective time step of ≈ 1 μs. Deviations from charge neutrality resulting from the acceleration are accounted for by renormalizing the densities of negatively charged species in each cell to equal the sum of positively charged densities;

$$N_j^-(r,z)\rightarrow N_j^-(r,z)\frac{\sum_k N_k^+(r,z)}{\sum_k N_k^-(r,z)}. \quad (26)$$

After the acceleration, the surface charge densities are "cleared" on dielectric surfaces, and the FKS is restarted with these new estimates for densities. This procedure has the effect of restarting the calculation with a better "first guess" for the densities. After a series of acceleration steps during an iteration, the continuity and Poisson's equations are integrated without acceleration. On a final set of iterations, the equations are integrated without acceleration until all species densities converge to the quasisteady state. Acceleration can optionally be performed on a computational cell-by-cell basis.

The 2D forms of the continuity equations and the semi-implicit form of Poisson's equation were discretized using the finite-difference donor cell technique. The electric fields were defined at cell boundaries, and densities and potentials were defined at cell centers. All fluxes were defined at the cell boundaries.

The FKS module has the capability to address rf capacitive biasing of the substrate and capacitive coupling from the coil. 2D parallel-plate capacitively coupled discharge models have recently been developed by Tsai and Wu[18], Dalvie *et al.*,[19] Economou *et al.*,[20] and Pak and Rielly.[21] Our model differs from those works primarily in the manner of obtaining electron impact rates. Tsai and Wu, Dalvie *et al.*, and Economou use three-moment fluid equations to generate a local electron energy. Electron impact rate coefficients are obtained by either using analytic expressions; or using parameterized solutions of Boltzmann's equations for the electron energy distribution. Our method of solution is similar to that of Pak and Rielly who use a Monte Carlo fluid hybrid model.

Radio-frequency biasing of the substrate is included in the FKS by specifying a sinusoidally varying potential on the lower boundary of the reactor in the solution of Eq. (22). Capacitive coupling can also occur from the antenna due to the inductive voltage drop across the coil. Capacitive coupling from the coil is handled in a similar fashion to that for the substrate bias. A sinusoidal potential is specified as a potential boundary condition on the top of the dielectric roof. We assume the coil is powered at the center tap and grounded at the outer radius. The potential boundary condition is then

$$\Phi(r,H+d,t)=V_0\left(\frac{r}{R}\right)\sin(\omega_c t+\gamma), \quad (27)$$

where d is the thickness of the dielectric. V_0 is the inductive voltage drop across the coil, ω_c is the applied frequency (rad/s), and γ is the phase offset relative to the rf bias of the substrate. Commercial etching tools often employ the same frequency for the coil voltage and the substrate bias. It is also common, however, for the frequency of the rf bias to the substrate ω_s to be different and typically lower than the frequency of the voltage applied to the coil.[28]

When a rf bias is applied to the substrate or there is capacitive coupling from the coil, the ICP discharge is functionally an asymmetric rf discharge. As a result, a dc bias can be generated on the substrate. To account for the dc bias, we use a simple circuit model which consists of a capacitor in series with the rf voltage source on the substrate. We specify, as input to the model which surfaces are considered the "lower electrode," and which surfaces are considered the "upper electrode." The dc bias on the lower electrode is calculated by integrating (in time) the net current flowing to the electrodes;

$$V_{dc}=\frac{1}{C_0}\int\left\{\int_{\text{upper}}\left[\epsilon_0\left(\frac{d\mathbf{E}_s}{dt}\right)+\sum_j eq_j\phi_j\right]\hat{n}\, dA - \int_{\text{lower}}\left[\epsilon_0\left(\frac{d\mathbf{E}_s}{dt}\right)+\sum_j eq_j\phi_j\right]\hat{n}\, dA\right\}dt, \quad (28)$$

where C_0 is capacitance in series with the voltage generator and the integrals are over the upper and lower electrode surfaces. The terms in the integrals are for the displacement current and conduction currents, respectively, and only the normal component of the current to the surface is included. In the quasisteady state, the dc bias is not a function of C_0. In the model, the bias asymptotically approaches its quasisteady state value. The value of C_0 only determines the time required to reach the quasisteady state value of V_{dc}. To speed convergence of V_{dc} we linearly ramp C_0 from smaller (10s pF) to larger (10s nF) values over the first half of the simulation.

D. Plasma chemistry Monte Carlo simulation

The FKS does not resolve energy dependent fluxes of ions and radicals. The purpose of the PCMCS is generate these

fluxes as a function of (r,z). The PCMCS is similar to the model described in Refs. 17 and 29. It will be discussed in detail in a subsequent publication, and so will be only briefly described here.

At the termination of the hybrid model described above, we have generated electron impact source functions $S_j(r,z)$ for species j and time averaged electrostatic fields $E_s(r,z)$. These values are used as input to the PCMCS. In the PC-MCS, pseudoparticles representing ions, excited states, and neutral radicals are launched from random locations in (r,z) computational cells in the reactor based on the magnitude of $S_j(r,z)$. Pseudoparticle l for species j is given a statistical weighting

$$w_{jl}=S_j(r,z)v(r,z)/M_j(r,z), \tag{29}$$

where $v(r,z)$ is the volume of the computational cell centered on (r,z) and $M_j(r,z)$ is the number of pseudoparticles of type j launched from the computational cell. The weighting w_{jl} has units of (atoms or molecules) s^{-1}. If a source of a pseudoparticle at a particular location is negative, we introduce an appropriate spatially weighted collision frequency which removes those pseudoparticles.

The trajectories of the pseudoparticles are integrated in time using Monte Carlo techniques similar to those used for the EMCS and described in Sec. II B. All pertinent collisions of ions and radicals (e.g., charge exchange, Penning reactions, chemical reactions) are implemented on a particle–mesh basis. That is, the time to the next collision is determined from Eq. (8) and the type of collision is determined using the probability arrays defined by Eq. (4) and the algorithm described by Eq. (9). The collision frequency for a particular process j may be a function of position because the density of the collision partner is a function of position. To account for this possibility, the collision frequency for species k used in Eq. (3) is defined as

$$\nu_{ijk}=\left(\frac{2\epsilon_i}{M_k}\right)^{1/2}\sigma_{ijk}\max[N_j(r,z)], \tag{30}$$

where M_k is the mass of species k, i denotes the energy, and j the collision partner having density $N_j(r,z)$. (An arbitrary number of collisions can occur with each species. That additional indice is suppressed here.) The max function denotes that the maximum density of N_j in the reactor is used to formulate the collision frequency. When a particular collision is selected, another random number $r=(0,1)$ is selected. If

$$r\leq\frac{N_j(r,z)}{\max[N_j(r,z)]}, \tag{31}$$

then a real collision takes place. If the inequality does not hold, then the collision is null.

Statistics for the density of each species are collected after updating the trajectory of every pseudoparticle. After each integration step, the statistically derived density for species j, $N_j(r,z)$ is incremented

$$N_j(r,z)\rightarrow N_j(r,z)+\frac{w_{jl}\Delta t(r,z)}{v(r,z)}, \tag{32}$$

where $\Delta t(r,z)$ is the time that the pseudoparticle spends in computational cell (r,z) during the trajectory. We optionally used finite sized particles. The trajectories of the pseudoparticles are advanced until the pseudoparticle is consumed by a reaction, sticks to a wall or leaves the chamber through a pumping port. All particles leaving surfaces as a result of a nonsticking collision are given a Lambertian distribution of velocities (diffuse reflection) with grazing angles ($<10°$) excluded to account for surface roughness. The energy of the reflecting pseudoparticle is either randomly selected from a thermal distribution at the wall (or substrate) temperature; or is a specified fraction of the incident energy.

When the pseudoparticle undergoes a collision, the identity of the pseudoparticle is changed and additional pseudoparticles for reaction partners are added as necessary. For example, the charge exchange collision of an argon ion pseudoparticle

$$Ar^+ + CF_4 \rightarrow CF_3^+ + F + Ar \tag{33}$$

results in the identity of the Ar^+ pseudoparticle being changed to Ar; and psuedoparticles being launched for CF_3^+ and F. The weight w_l of the reactant pseudoparticle is assigned to all product pseudoparticles.

When all pseudoparticles and their progeny are collected, the collision frequencies for all species are updated using the most recently calculated values of $N_j(r,z)$. The calculation is then repeated and iterated until the computed fluxes and $N_j(r,z)$ converge. In this fashion, radical–radical, radical–ion, and ion–ion collisions can be included in the simulation on a particle–mesh basis. Appropriate adjustments are made in the source functions for unaccounted depletion of the feedstock gases. Typically, 10 000–30 000 pseudoparticles are used over 10–20 iterations to obtain converged densities.

The pressures of interest are in the quasimolecular flow regime. Direct Monte Carlo simulations (DMCS) of low pressure chemical vapor deposition (LPCVD) in a similar pressure regime have shown that significant pressure gradients can be sustained. To account for pressure driven advective flow in the PCMS, the following algorithm is used.[29]

Prior to executing the model, the advective flow field in the reactor is calculated assuming that the conventional hydrodynamic continuity and momentum equations are valid. We acknowledge that the advective flow field is only approximately represented in this manner at pressures of a few mTorr. The advective flow field is not directly used to describe transport of radicals, but rather provides for momentum transfer to those radicals.

If a gas phase, the collision is an elastic momentum transfer collision, we assume that the momentum of the collision partner is given by the sum velocity components of the advective flow field at that location and a randomly selected thermal velocity chosen from a Maxwell–Boltzmann distribution. The collisional exchange of momentum is then calculated using standard elastic collision theory. In this manner the pseudoparticle "senses" the net advective flow field after a statistically meaningful number of collisions. At pressures of 10s mTorr the pseudoparticles have enough collisions to nearly come into equilibrium with the advective flow field. This algorithm is described in more detail in Ref. 29.

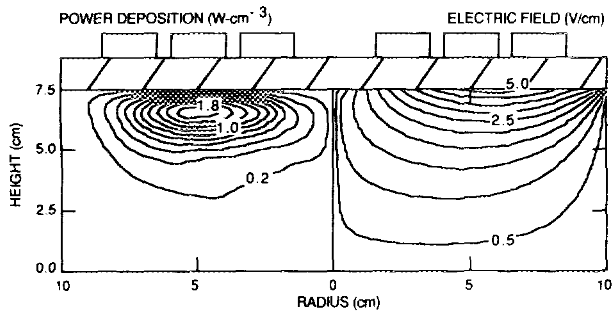

FIG. 3. Power deposition and amplitude of the azimuthal electric field for an ICP discharge sustained in Ar at 10 mTorr. The skin depth for the electric field is $\approx$1.5 cm. This results in a toroidal power deposition which peaks below the dielectric.

III. ICP PLASMA PARAMETERS

In this section, we will discuss results from the model for ICPs sustained in pure gases and gas mixtures. We will also compare ICPs with and without a rf bias applied to the substrate; and with and without using a magnetic bucket. The pressure range investigated was 5–15 mTorr and the inductively coupled power deposited in the gas was nominally 500 W. The dimensions of the reactor are 20 cm (diameter)$\times$7.5 cm (tall). The dielectric roof is 1.0 cm thick. All applied rf potentials are at a frequency of 13.56 MHz. In the absence of rf biasing of the substrate, the sidewalls and substrate are metal and grounded. Radio-frequency voltage is applied to the center tap of the coil and the outer tap is grounded. We will investigate three systems: Ar, O_2, and $Ar/CF_4/O_2$ =85/13/2. These systems are representative of nonattaching and attaching gases; and a gas mixture used for etching of SiO_2. In describing cases below, ICP refers to a discharge that is sustained by only the inductively coupled azimuthal electric field; that is, no capacitive coupling from the coil is allowed. ICP with rf biasing refers to a discharge which is sustained by the inductively coupled azimuthal electric field as in the ICP case and which also has a capacitively coupled rf bias applied to the substrate. Capacitive coil coupling refers to cases where we allow the inductive voltage drop across the coil to couple to the plasma.

The behavior of ICP reactors is largely determined by the spatial variation and penetration of the azimuthal electric field. The amplitude of the azimuthal electric field and the inductively coupled power deposition are shown in Fig. 3 for a typical ICP discharge sustained in Ar at 10 mTorr. The shape and amplitude of the electric field is essentially the same as that measured by Hopwood *et al.*[12] The vacuum electric field is zero on the axis, outer radius, and substrate. The maximum azimuthal electric field is 5 V cm^{-1} just below the dielectric roof. The coil current as an amplitude of 38 A. The finite skin depth (1–2 cm for 10^{11}–10^{12} cm^{-3} electron density) significantly reduces penetration of the electric field into the bulk of the plasma.[12] The immediate consequence of the symmetry of the electric field and the finite penetration of the electric field is that the inductive power is deposited within a few centimeters of the dielectric roof. In this case, the peak power deposition is $\approx$2 W cm^{-3} at 1 cm below the dielectric. This results in a toroidally shaped region in which the majority of direct electron impact excitation from the ground state occurs.

The local power deposition shown in Fig. 3 is

$$\mathrm{Re}(\sigma)E^2=\frac{[e]q^2}{m_e\nu_m(1+\omega^2/\nu_m^2)}E^2, \tag{34}$$

where ν_m is the momentum transfer collision frequency and ω is the rf frequency. The plasma conductivity is maximum in the bulk plasma and decays towards the dielectric while the electric field is maximum at the dielectric and decays towards the plasma. Since the conductivity determines the penetration of the electric field, small variations in the slopes of either of the electric field or conductivity results in large variations in the power deposition; or large variations in coil current for a given power deposition. The sensitivity of electron density and plasma potential to variations in the penetration of the electric field is perhaps best illustrated by their time evolution during iterations between the EMM, EMCS, and FKS modules (see below). There is also a component of stochastic heating produced by the oscillating nature of $E_\theta(r,z,\phi)$.[12,30,31] Although this heating is captured in the EMCS, it does not appear in Fig. 3. Stochastic heating in ICPs will be discussed in detail in a subsequent publication.

The mechanics of the iterative and acceleration algorithms used in the model are illustrated in Fig. 4, where the time evolution of reactor averaged electron density, negative ion density, and plasma potential are shown for a oxygen ICP discharge with a rf bias at 5 mTorr. The simulation begins by executing the EMM and EMCS. The FKS is then executed for the equivalent of 20 rf cycles. The first 7 of these cycles are accelerated. The FKS is executed for 1 rf cycle, an acceleration operation is performed, and the FKS calculation is restarted from charge neutrality with updated densities. Results from the FKS are cycled back to the EMM and EMCS every 1 μs. The acceleration operations are terminated at 10 μs.

The electron densities evolve from an initially low guess. The low electron density and a resulting low conductivity results in a large degree of penetration of the electric field. This produces commensurately large ionization rates. On successive iterations the increase in electron density resulting from the initially large ionization rates increases the conductivity and the field penetration decreases. This results in a lower rate of ionization and eventual decay of the plasma. There is some unavoidable amount of overshoot which occurs, but the electron density evolves to a quasisteady state value of $\approx 4.2\times10^{10}$ cm^{-3}. The density of the negative ions smoothly evolve from initially low values to their quasisteady state since their residence time in the plasma exceeds the time for an iteration. Iteration to iteration variations in sources for negative ions are therefore averaged to some degree. The response of the plasma potential from iteration to iteration largely reflects the behavior of the electron temperature. Early iterations where the electron density is low and field penetration is large results in a high electron temperature and commensurately large plasma potential. The plasma potential evolves to a quasisteady state of $\approx$17.5 V as the field penetration stabilizes.

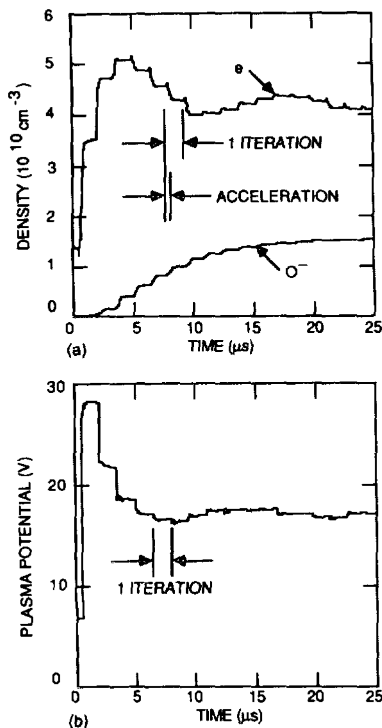

FIG. 4. Demonstration of the iterative and acceleration algorithms used in the hybrid model for an ICP discharge (13.56 MHz) sustained in O_2 at 5 mTorr. (a) Electron density and O^- density; and (b) plasma potential. The hybrid model is iterated 18 times. The FKS is performed for 20 cycles each iteration, with acceleration performed the first 7 cycles of each iteration. Acceleration is ceased at 10 μs. An initially low guess for the electron density results in a low conductivity and large field penetration. This produces large ionization rates. The plasma density overshoots its quasicontinuous value as the electric field penetration decreases.

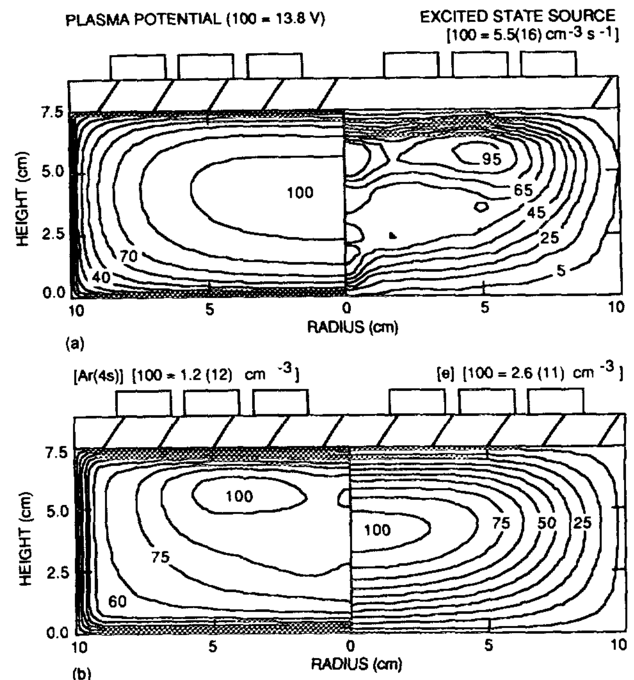

FIG. 5. Plasma parameters for an ICP discharge (13.56 MHz) sustained in Ar at 10 mTorr. (a) Plasma potential and rate of production of Ar(4*s*); and (b) Ar(4*s*) and electron density. The Ar(4*s*) density is somewhat localized due to its rapid ionization or superelastic relaxation after being formed by electron impact of the ground state. [Note: The quantity in parenthesis at the top of each figure is the maximum value of the variable. The contour labels denote the percentage of the maximum value. The label 1.2(12) denotes 1.2×10^{12}, typical for all labels.]

A. Ar ICP discharges

Argon ICP discharges were investigated as being typical of electropositive plasmas, where multistep ionization is important. The electron density (equal to the Ar^+ density), Ar(4*s*) density, plasma potentials, and rate of excited state production are shown in Fig. 5 for an Ar ICP discharge at 10 mTorr. (See Fig. 3 for the electric field and power deposition.) The source of ionization from the ground state and Ar(4*s*) states of Ar are shown in Fig. 6. The maximum plasma density is $\approx 2.3\times10^{11}$ cm^{-3}, whereas the maximum Ar(4*s*) density is $\approx 1.1\times10^{12}$ cm^{-3}. The plasma density, Ar(4*s*) density, plasma potential and ionization of ground state Ar are all displaced towards the top of the reactor, where the dominant power deposition occurs. The peak in the plasma potential should coincide with the peak in the ionization which, for the ground state (threshold 16 eV), is just under the dielectric. The ionization, though, has large contributions from electron collisions with Ar(4*s*) which has a threshold of 4 eV. This source is substantially more uniform thoughout the plasma compared to ground state ionization due to the diffusion of Ar(4*s*) from its source, which is similar in shape to that for ground state ionization, and the abundance of lower energy electrons throughout the plasma.

The sheath is not fully resolved in these calculations, however we feel that the pertinent physics is nevertheless being captured. During our model development we used an analytic sheath model similar to that described in Ref. 32 for our model of high plasma density pulse power switches. Assuming the sheath is collisionless, we placed an analytically derived potential drop (as given by a Child–Langmuir expression) between the last computational mesh point and the surface to represent the sheath. Positive ions pass through the sheath unhindered, whereas a fraction of the electron flux (or negative ion flux) is reflected as specified given by Boltzmann statistics.

We found that the ICP plasma parameters are essentially unchanged with or without the analytic sheath model. The

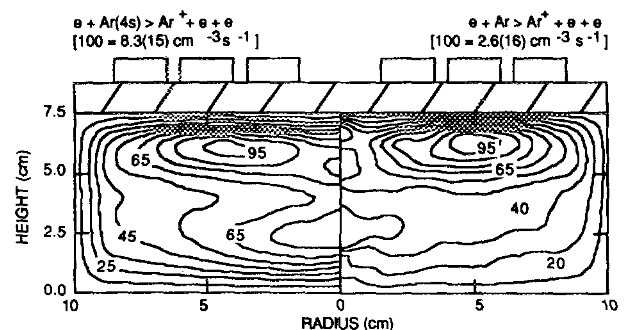

FIG. 6. Electron source functions by electron impact for ionization of (left) Ar(4*s*) and (right) ground state Ar. The multistep ionization of Ar(4*s*) is more uniform due to its lower threshold energy. (See Fig. 5 for contour labeling scheme.)

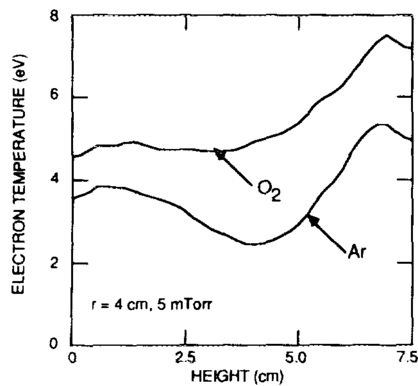

FIG. 7. Electron temperature as a function of height (radius =4 cm) in ICP discharges in 5 mTorr of Ar and O_2. The electron temperature peaks under the substrate where the power deposition is largest. The electron temperature of the Ar ICP is depressed in the middle of the plasma due to rapid power loss to collisions with Ar (4*s*).

plasma density and peak plasma potential differed by only a few percent. The most noticeable difference was that the potential within 0.5–1 cm of the sheath (approximating the presheath) was flatter when using the analytic sheath model, since more of this voltage now appeared across the analytic sheath. We attribute this behavior to the fact that the ambipolar fields must contain the plasma, and the plasma potential is determined largely by the ratio of electron and ion temperatures. Another convenient set of circumstances is that in high plasma density, low gas pressure plasmas the sheath is thin and collisions are sparse thereby assuring that the sheath is basically collisionless. As long as the sheath is collisionless, the necessity to fully resolve it diminishes.

The electron temperature (defined as $0.67\langle\epsilon\rangle$) as obtained from the EMCS as a function of height ($r=4$ cm) is shown in Fig. 7 for a pressure of 5 mTorr. For these conditions, T_e is actually depressed towards the center of the reactor. The electron temperature should logically peak towards the top of the reactor where the power deposition is large and to some degree does.[15] The depression in the electron temperature results from high rates of inelastic collisions with Ar(4*s*) in the center of the plasma. The power loss of electrons through collisions with Ar(4*s*) is large due to the large cross section for Ar(4*s*)→Ar(4*p*) transitions and for ionization. There is also a component of diffusion heating in the electron temperature profile. Diffusion heating results from secondary electrons produced in the sheaths or presheaths, which are then accelerated down the ambipolar potential hill towards the center of the plasma.[33] This effect may be exaggerated in our calculations due to our broadening of the presheath discussed above.

The spatial dependence of T_e for an Ar ICP discharge differs from the electron temperature in an O_2 discharge at the same power and pressure, which is also shown in Fig. 7. The rate of inelastic loss from electronic excited states is significantly less in O_2 than in Ar due to the lack of a high lying metastable states in O_2. The electron temperature in the O_2 discharge is maximum at the top of the discharge, where power deposition is maximum and monotonically decreases towards the substrate.

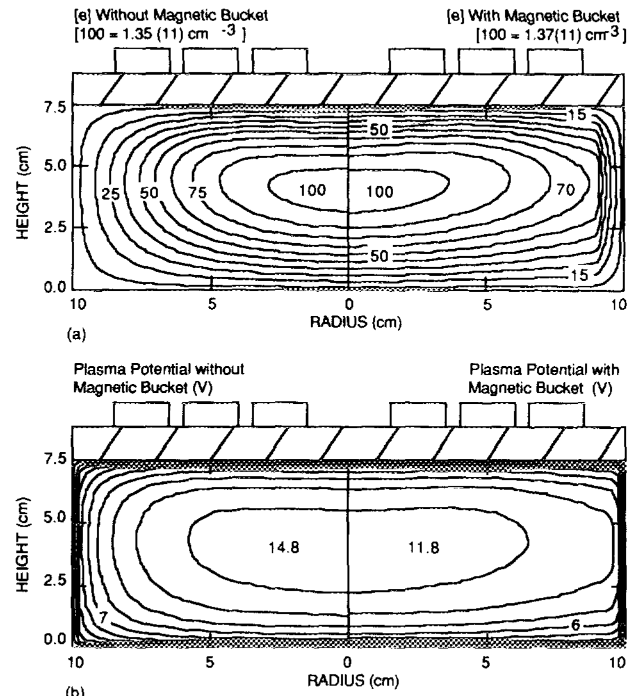

FIG. 8. Plasma parameters for ICP discharges in Ar (5 mTorr) with and without a magnetic bucket; (a) electron density and (b) plasma potential. Using the magnetic bucket lowers the plasma potential; and makes both the plasma density and plasma potential more uniform in the radial direction. (See Fig. 5 for contour labeling scheme.)

The electron density and plasma potential are shown in Fig. 8 for a 5 mTorr Ar ICP discharge with and without using a magnetic bucket. The peak density in both cases is $\approx 1.4\times10^{11}$ cm^{-3}. The effect of the magnetic bucket is to make both the electron density and plasma potential more uniform, and so the total plasma inventory is larger when using the magnetic bucket even though the peak plasma density is the same. Using electric probes, Hopwood measured ion saturation current in 5 mTorr O_2 discharges with and without a magnetic bucket.[13] With magnetic confinement, the plasma was uniform to within a few percent over 20 cm of the diagonal of a 27×27×13 cm reactor. The ion saturation current fell to nearly half of its value in this distance in the absence of magnetic confinement. These values are commensurate with our results. The radial walls are only 40% of the surface area of the reactor; and the axial diffusion length is smaller than that in the radial direction. The density gradients in the axial direction near the radial wall increase with the magnetic bucket relative to the unmagnetized case. This tends to increase the axial loss of plasma to the upper and lower surfaces at larger radii. The end result is that the bucket is not particularly effective at changing the plasma density at the center of the plasma.

The improved radial uniformity of charged species which results from using the magnetic bucket arises from a decrease in the radial mobility of electron through the cusp fields. This has the effect of increasing the effective diffusion length of the reactor in the radial directions. The ions are only mildly magnetized and so, in some cases, have a higher mobility than the electrons through the cusps. We have ob-

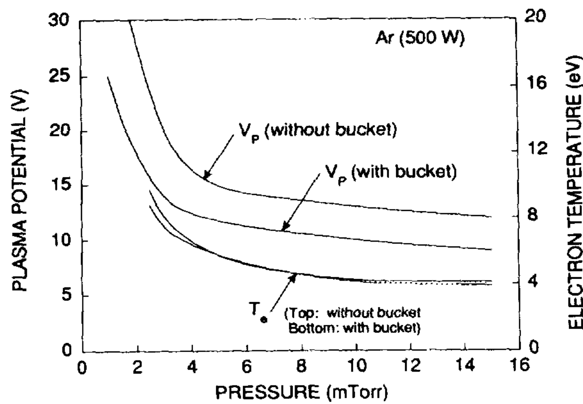

FIG. 9. Plasma potential and electron temperature as a function of gas pressure in Ar ICP discharges with and without the magnetic bucket. The plasma potential with the magnetic bucket is many volts lower. Both the plasma potential and electron temperature rapidly increase below 4–5 mTorr.

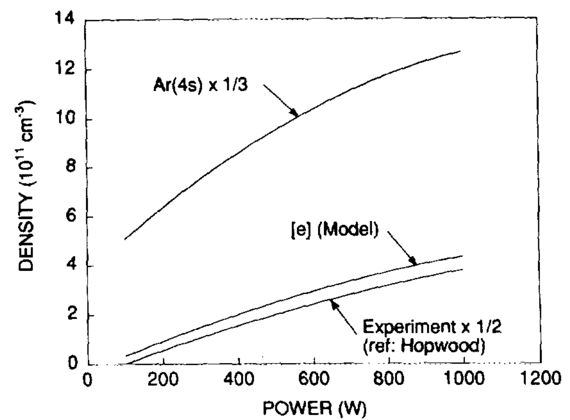

FIG. 10. Electron density and Ar(4s) density as a function of power deposition in Ar ICP discharges at 5 mTorr. Experimental results are from Hopwood *et al.* (Ref. 13).

served positive charging of the radial dielectric walls at low pressures when the mobility of the ions exceeds that of the electrons through the cusps.

The maximum plasma potentials and electron temperatures in Ar ICP discharges are shown in Fig. 9 as a function of pressure with and without the magnetic bucket. The plasma potential increases with decreasing pressure, agreeing with experiments,[10,11] which generally tracks the reactor averaged electron temperature. There is a large increase in the plasma potential at pressures <5 mTorr which is similar in behavior to plasma potentials measured in ECR reactors.[34] Experimentally, in ICP discharges this upturn occurs at ≈ 2 mTorr.[10,11] The plasma potential is smaller when using the magnetic bucket, a consequence of the lower rate of electron loss afforded by the cusp fields, while the electron temperature does not significantly change.

The peak Ar(4*s*) and electron densities as a function of power for a 5 mTorr Ar ICP are shown in Fig. 10 along with Hopwood's experimental results for similar conditions.[13] Consistent with Hopwood's results, we find a nearly linear increase in both electron and Ar(4*s*) densities with increasing power deposition, and a threshold inductively coupled power of ≈ 100 W below which the discharge cannot be sustained. Our predictions for electron density are about half those of Hopwood's, a difference we attribute to differences in reactor geometry.

B. O_2 ICP discharges

The electron and ion densities, plasma potential, and electron source for a 10 mTorr oxygen ICP with a magnetic bucket are shown in Fig. 11. The electron source has an off-axis maximum similar to the Ar discharge. The O_2^+ density and plasma potential also have an off-axis maxima coinciding with the toroidal power deposition. The maximum plasma potential is 17.5 V, while the potential on the axis is smaller by ≈ 1.7 V. These trends agree with the ion saturation current probe measurements made by Hopwood *et al.*[13] which show clear off-axis maxima for a 500 W, 5 mTorr O_2 ICP.

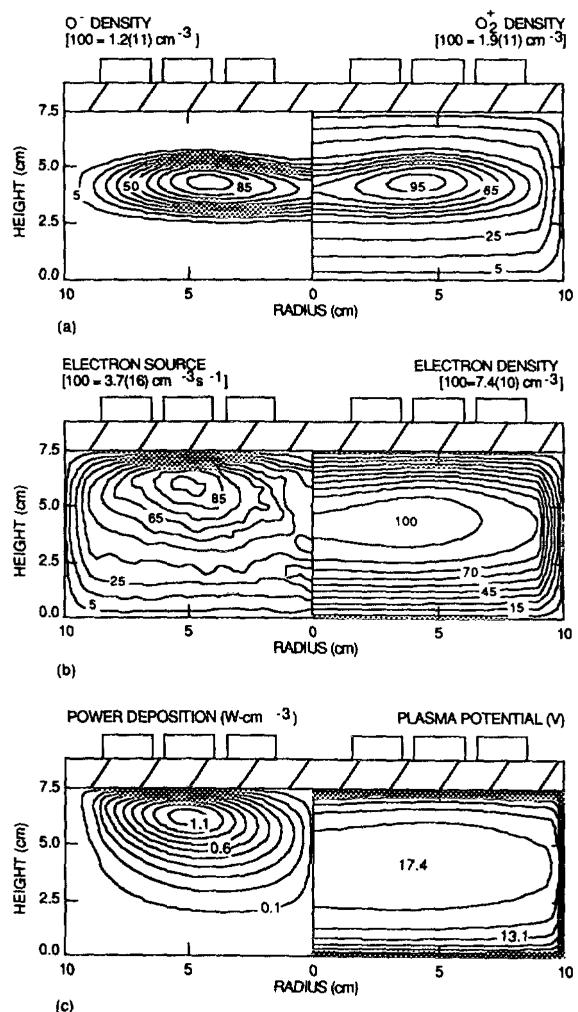

FIG. 11. Plasma parameters for an ICP discharge sustained in 10 mTorr O_2. (a) O^- and O_2^+ densities; (b) electron source and electron density; and (c) power deposition and plasma potential. ICP discharges sustained in molecular attaching gases can display off-axis maxima in plasma potential and ion densities. Negative ions will pool at the maximum in the plasma potential. (See Fig. 5 for contour labeling scheme.)

Off-axis maxima in ion density results in a net flux of ions towards the axis. This can only be sustained if there is a "sink" on the axis. In molecular gases, attachment and dissociative recombination provide a volumetric sink which can sustain off-axis maxima; and therefore these structures are more likely to be found in molecular gases. However, in 2D systems, radial fluxes from off-axis maximum can be redirected towards the upper and lower boundaries and thereby sustain the off-axis maxima. There is, then, no *a prior* reason why these maxima cannot be sustained in atomic gases other than the dominance of more spatially uniform multistep ionization processes and larger rates of diffusion.

The negative ion density for the 10 mTorr O_2 discharge has a maximum value of $\approx 1.1 \times 10^{11}$ which exceeds the electron density. However on a reactor averaged basis the electronegativity (negative ion density/electron density) is ≈ 0.2. This is small compared to typical RIE discharges sustained at higher pressures (10s–100s mTorr) and lower plasma densities (10^9–10^{11} cm^{-3}). We have found that the electronegativities of low pressure, high plasma density discharges are lower than conventional RIE discharges. This results from the production of negative ions scaling as $[e]N$ (N is the neutral gas density), whereas the destruction mechanism scales as $[N^-][N^+]$. Therefore, low pressures and high plasma densities favor destruction processes over production processes. In cases where there is significant dissociation of the attaching feedstock molecule, the negative ion density will be small as well.[35]

In this model, the O^- ions are essentially at room temperature. Since they are not energetic enough to scale the plasma potential to higher values, the O^- ions pool at the peak of the plasma potential. A small amount of noise in the O^- density is caused by ≈ 0.05 V noise in the plasma potential resulting from the Monte Carlo generated source functions. The off-axis maximum in O^- is, in fact, a good indication of the location of maximum in the plasma potential. Since the plasma potential of a purely inductively coupled discharge is quiescent, both the plasma potential and distribution of negative ions resemble that of a positive column discharge.

Barnes *et al.*[10] have performed probe measurements of electron and ion densities in oxygen plasmas at higher powers (1000 W). They found that the electron density at the center of the reactor had a maximum value of 2.7×10^{11} at 2 mTorr, and decreased to 1×10^{11} cm^{-3} at 10 mTorr. The negative ion densities were two to three times the electron density, while the plasma potential was ≈ 15 V. A comparison between the electron density data of Barnes *et al.*[7] and our model is shown in Fig. 12. Our results show a similar trend in that there is a maximum in electron density of approximately the same value, but at a higher pressure. For these cases we assumed that all of the power is inductively coupled into the plasma. A portion of the differences between calculated and experimental values for ion densities could be attributed to capacitive coupling from the coils which is not accounted for in the model or to inadequate depletion of O_2 in the model.[35] The effects of capacitive coupling will be discussed below.

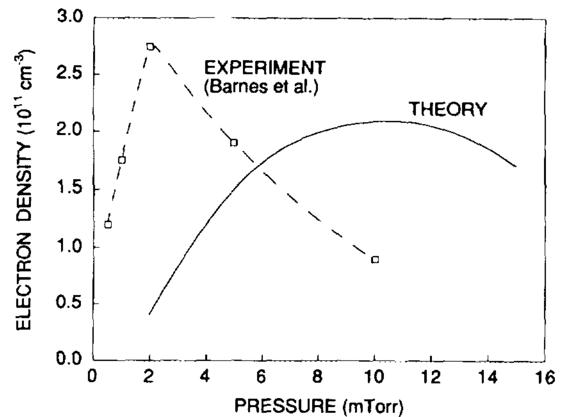

FIG. 12. Electron densities in 1000 W ICP discharges including a comparison to electric probe measurements of Barnes *et al.* (Ref. 10).

C. $Ar/CF_4/O_2$ discharges with and without rf bias

$Ar/CF_4/O_2$ gas mixtures are of interest as candidates for etching of SiO_2. These mixtures have both Penning and multistep ionization, as well as attachment, and so are typical of more complex plasma chemistries. The reactor averaged electron density for $Ar/CF_4/O_2$, Ar, and O_2 gas mixtures are shown in Fig. 13(a) as a function of pressure for a power deposition of 500 W. The densities of negative and positive ions for the $Ar/CF_4/O_2$ gas mixture are shown in Fig. 13(b). In gas mixtures in which multistep ionization and Penning reactions are important, the electron densities are higher and they increase with increasing pressure over this range of pressure. These results are in general agreement with probe measurements by Hopwood [also shown in Fig 13(a)]. In these cases, the density of Ar(4*s*) increases with increasing pressure largely due to the reduction in the loss by diffusion. This affords a larger source of ionization for a given power. In O_2 plasmas, the lack of multistep and Penning processes result in a nearly constant electron density, decreasing towards higher pressures where more power is dissipated in nonionizing collisions.

The dominant positive ion is Ar^+ even though there is charge exchange to CF_4 and O_2. The mean-free-path for Ar^+ nonsymmetric charge exchange is sufficiently long at low pressures that the majority of Ar^+ is lost by diffusion. The Ar^+ density decreases relative to CF_3^+ at high pressures due to increased rates of charge exchange to CF_4. At pressures typical of RIE discharges, CF_3^+ will be the dominant ion. (O_2^+ has a small density primarily because the mole fraction of O_2 is small.) Throughout this pressure range, the negative ion density is surprisingly low. This behavior is caused, in part, to the scaling of negative ion sources and sinks discussed above, and the small mole fractions of CF_4 and O_2. The threshold for dissociative attachment in CF_4 is 4.4 eV. The electron temperature in these mixtures (maximum value of 3.8 eV at 10 mTorr) is relatively low, a result of large amounts of Penning and multistep ionization. Therefore, the low temperature results in a relatively low rate of attachment to CF_4.

One of the features of ICP discharges is that the electron source generated by the azimuthal electric field can, in prin-

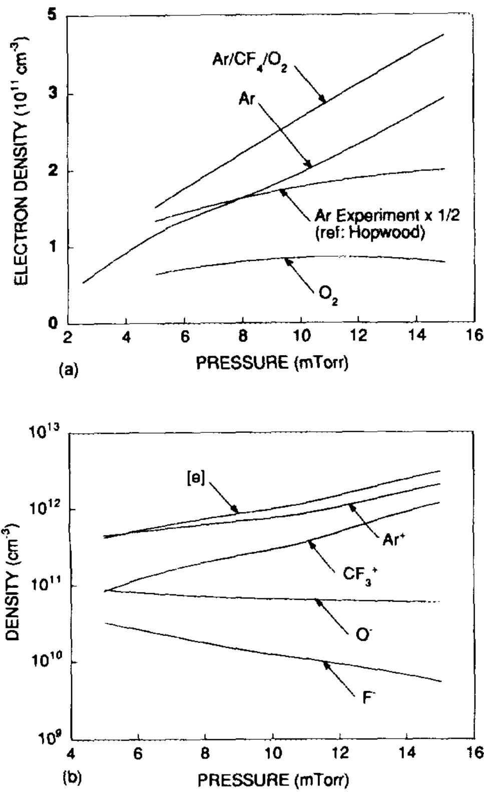

FIG. 13. Plasma densities as a function of gas pressure. (a) Electron density in Ar/CF_4/O_2, Ar, and O_2 discharges; (b) charged particle densities in the Ar/CF_4/O_2 discharges. In Penning mixtures or mixtures with large cross sections for multistep ionization, plasma densities increase with increasing gas pressure over this range. The CF_3^+ density increases relative to Ar^+ with increasing gas pressure due to the increasing rate of charge exchange of Ar^+ with CF_4. The experimental results are from Hopwood *et al.* (Ref. 13).

ciple, be decoupled from ion acceleration to the substrate produced by a capacitively coupled rf bias. In reactors in which the effective areas of the powered and grounded electrodes differ, a dc bias also contributes to ion acceleration. In addition to the controlled rf biasing of the substrate, capacitive coupling can also occur from the inductive voltage drop across the coils. This capacitive coupling manifests itself as a radially dependent potential on top of the dielectric. This differs from the rf biasing of the substrate which is equipotential across the radius. As a result, the capacitive coupling from the coil can distort the plasma potential in a different manner than the rf bias on the substrate.

We investigated the consequences of capacitive coupling in ICP discharges using Ar/CF_4/O_2 mixtures with 500 W inductive power, 75 V (amplitude) applied to the substrate at 13.56 MHz and using a magnetic bucket configuration.[36] The rf bias is uniformly applied to the lower substrate in these examples. The peak plasma potential as a function of time and the time averaged plasma potential are shown in Fig. 14 (15 mTorr). The upper electrode in this case was specified to be the sidewalls and upper dielectric. This asymmetry results in production of a -55 V dc bias. The peak plasma oscillates at the rf period. In the absence of the dc bias, the plasma potential would oscillate with an amplitude nearly equal to the applied bias. The dc bias "pulls" the plasma potential to

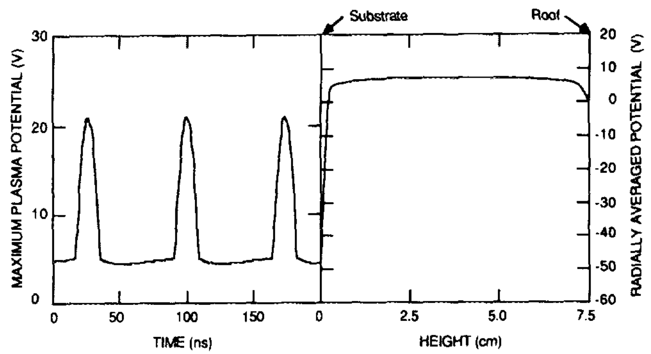

FIG. 14. Maximum plasma potential as a function of (left) time and (right) time averaged plasma potential as a function of height (radius =0). The gas mixture is Ar/CF_4/O_2 at 15 mTorr. A 75 V rf bias is applied to the substrate. A dc bias of -55 V on the substrate "pulls down" the plasma potential so its oscillation has an amplitude of only 20 V.

lower values, allowing excursions only when the applied rf potential exceeds the dc bias and floating potential.

The contribution of the rf bias is not limited to acceleration of ions. There is significant ionization which occurs from stochastic heating of electrons by the oscillating sheaths at all boundaries, and at the substrate in particular. Time averaged electron sources with and without an rf bias are shown in Fig. 15 for a 10 mTorr Ar/CF_4/O_2 mixture. The electron source is increased by stochastic heating of electrons by the oscillating sheath both under the dielectric, adding to the ionization generated by the azimuthal field, and at the substrate. The relative increase in ionization at the substrate is proportionally larger due to the larger excursions of the sheath potential.

The ICP reactor with a rf bias on the substrate resembles an externally sustained discharge. In conventional externally sustained devices, photoionization or an injected electron beam provides the base source of ionization or production of high lying metastables.[37] The bulk electric field in the plasma need only heat the electrons to subionizing energies (based on the ground state) as suited for the desired vibrational or electronic excitation. In the case of gas mixtures having long lived electronic states, the moderately heated electrons are well suited for second step ionization. The azimuthal electric field at the top of the reactor serves the role of an "external" source of ionization for the lower portion of the plasma. This source feeds electrons and metastables to the oscillating sheath near the substrate where they are heated and generate additional ionization.

The rf bias results in an increase in power deposition of 400 W, the majority of which is ion acceleration into the substrate. The additional power deposited in the plasma results in an increase in the electron and Ar(4*s*) densities of more than a factor of 2, as shown in Fig. 16. The location of the maximum of the Ar(4*s*) density is shifted towards the substrate with the rf bias, as is the electron density. Surprisingly, though, the bulk electron temperature does not dramatically increase. The tail of the electron energy distribution (EED), though, is lifted by the rf bias near the substrate, as discussed below. This accounts for the larger source of Ar(4*s*) near the substrate. Some of the increased heating of

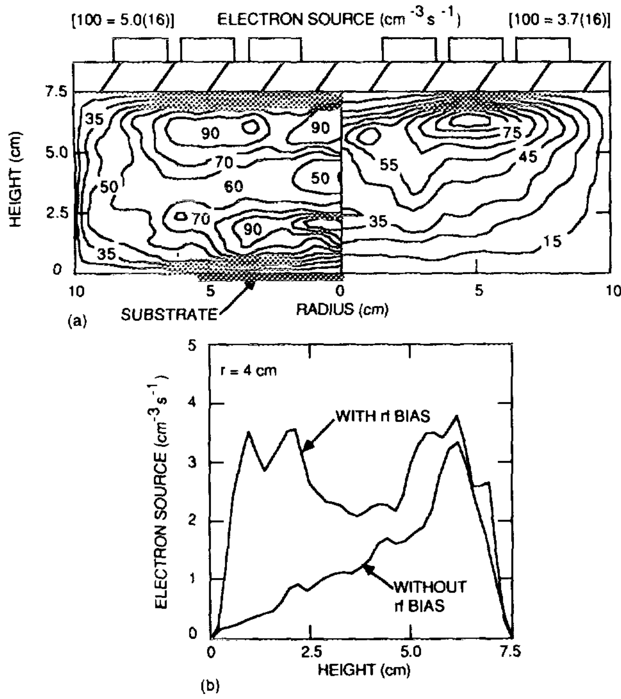

FIG. 15. Electron source functions for ICP discharges sustained in $Ar/CF_4/O_2$ (10 mTorr) with and without a rf bias on the substrate. (a) Electron sources a function of (r,z); and (b) electron source as a function of height at $r=4$ cm. The rf bias is efficient at heating the tail of the distribution thereby increasing the rate of multistep ionization. (See Fig. 5 for contour labeling scheme.)

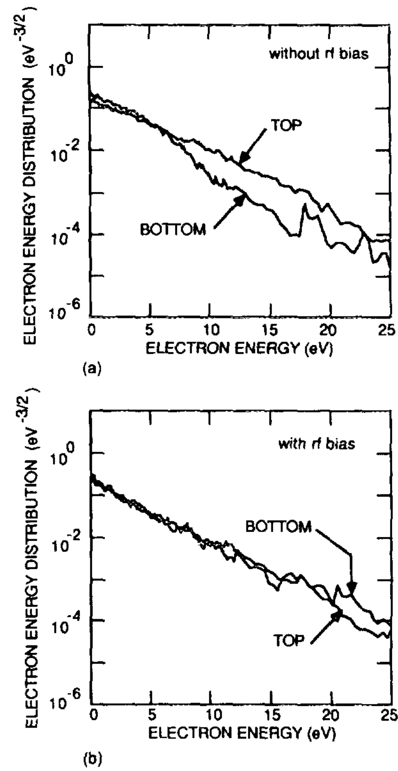

FIG. 17. EEDs for an ICP discharge in $Ar/CF_4/O_2$ at 5 mTorr. EEDs are shown near the dielectric (labeled top) and near the substrate (labeled bottom). Results are shown for discharges (a) with a rf bias and (b) without a rf bias. The rf bias raises the tail of the EED near the substrate.

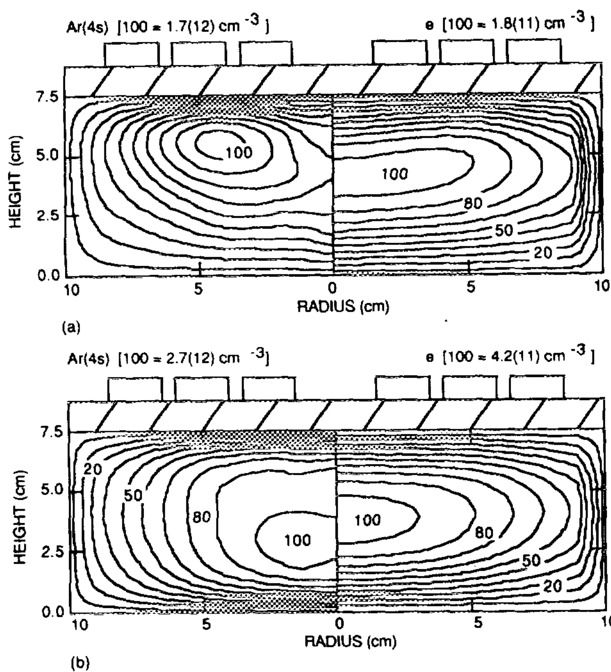

FIG. 16. Ar(4s) and electron density with and without a rf bias on the substrate for an $Ar/CF_4/O_2$ ICP discharge; (a) without a rf bias and (b) with a rf bias. The rf bias shifts the maximum in the density of Ar(4s) towards the substrate. (See Fig. 5 for contour labeling scheme.)

the EED is compensated by larger densities of Ar(4s) which efficiently extract power from the electrons by multistep electron collisions.

The effect of auxiliary heating by the rf bias on the EED is shown in Fig. 17. Here we see EEDs at the top (under the dielectric near the peak in the power deposition) and bottom (above the substrate) of the plasma with and without a rf bias. The gas pressure is 5 mTorr and gas mixture is $Ar/CF_4/O_2$. In the absence of the rf bias, the EED at the top of the plasma has a hotter tail and appears nearly Maxwellian. The EED at the bottom of the plasma is cooler and shows some cutoff character. With the rf bias, the EED at the top of the plasma does not appreciably change, while the tail of the distribution of the EED near the substrate is raised, and is nearly the same as that of the EED at the top of the plasma. The rf bias efficiently heats the tail of the distribution, much like an externally sustained plasma.

D. Capacitive coupling from the coil

The effect of capacitive coupling from the coil was investigated for $Ar/CF_4/O_2$ and Ar mixtures at 5 mTorr. As discussed in the previous section, capacitive coupling from the coil is accounted for by applying a time varying potential on the top of the dielectric. The coil voltage is also at 13.56 MHz, but 180° out of phase with the rf bias on the substrate. The coil is grounded at the outer radius and has a maximum amplitude of 75 V at the axis. The rf bias is applied to the central 12 cm of the substrate.

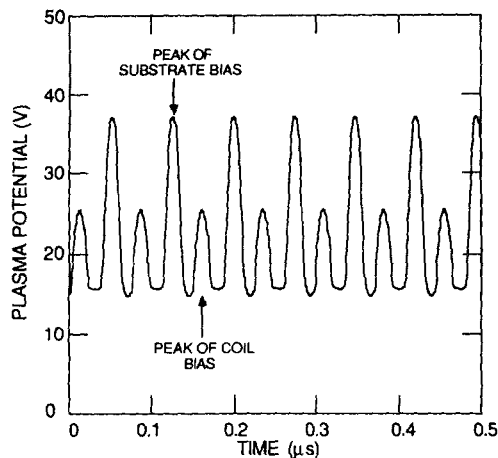

FIG. 18. Maximum plasma potential as a function of time for an $Ar/CF_4/O_2$ gas mixture at 5 mTorr when capacitive coupling from the coil is allowed. The coil bias is 180° out of phase from the substrate bias. The coil bias causes a lower excursion of the plasma potential due there being a voltage drop across the dielectric.

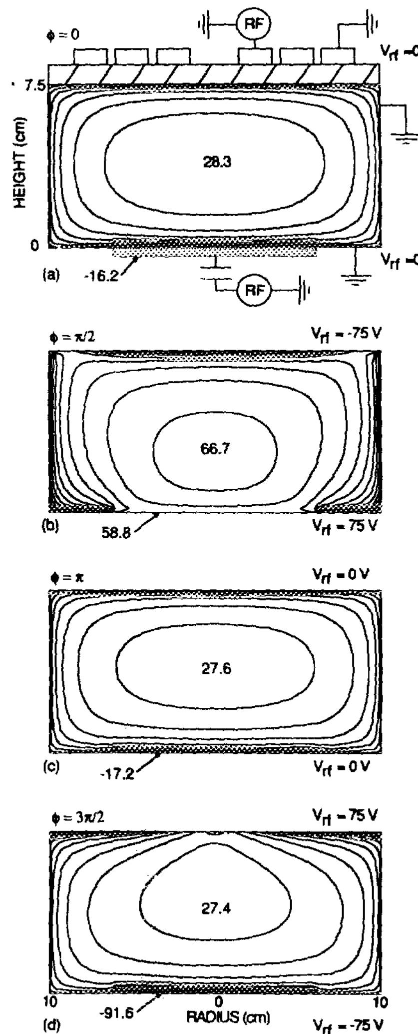

FIG. 19. Plasma potential in an Ar ICP discharge with a rf bias on the substrate and capacitive coil coupling (5 mTorr, 200 W ICP power). Potentials are shown at various phases during the rf cycle, (a) $\phi=0$, (b) $\phi=\pi/2$, (c) $\phi=\pi$, and (d) $\phi=3\pi/2$. The voltage on the substrate (bottom) and coil (top) are noted by the V_{rf} label. The nonuniform (with respect to radius) coil voltage causes nonuniform excursions in the plasma potential.

The peak plasma potential over a number of rf cycles is shown in Fig. 18. The dc bias on the substrate is −38 V. The peak plasma potential oscillates with twice the rf period. The plasma potential is maximum when either the substrate bias or coil bias are at their most positive values. The larger positive excursion corresponds to the maximum in the substrate bias. The smaller excursion of the plasma potential resulting from the coil bias is attributable to two effects. First, there is a voltage drop across the dielectric which reduces the applied contact potential. Second, since the coil bias varies as a function of radius, its effective value is weighted by the differential radial area. For a 75 V amplitude, the effective coil bias has a radially weighted value of ≈25 V.

The plasma potential is shown in Fig. 19 for four times during the rf cycle (phase $\phi=0$, $\pi/2$, π, $3\pi/2$) for the Ar discharge. The ICP power for this example is 200 W. In Fig. 19(a) ($\phi=0$), both rf biases are at zero. In Fig. 19(b) ($\phi=\pi/2$), the substrate bias is most positive and the coil bias is most negative. The plasma potential shows a great deal of structure. In Fig. 19(a), the substrate is at its dc bias of −16 V, which is a small fraction of the rf amplitudes. At $\phi=\pi/2$, the plasma potential is driven to its maximum value coinciding with the peak of the substrate bias. The coil bias is most negative near the axis, and the radially dependent sheath thickness and potential can be seen under the dielectric surface. The peak in the plasma potential is pulled towards the substrate where the applied potential is largest. At $\phi=\pi$, the biases are both zero, and the plasma potential is symmetric. At $\phi=3\pi/2$, the substrate is most negative pulling the plasma potential above the substrate to −92 V. The coil bias is most positive near the axis and this pulls the plasma potential to larger positive values. However, the plasma is able to shield the locally high surface potential near the center of the plasma from locations at larger radii. The spatial dynamics of the plasma potential are greater at lower gas pressures, lower power deposition and lower plasma densities.

E. Ion energy and radical distributions

Using electric fields and ion sources from the hybrid model, ion energy fluxes to the substrate were calculated using the PCMCS module. The ion energy distributions (IEDs) for Ar^+ and CF_3^+ incident on the substrate (averaged over the radius) are shown in Fig. 20(a) for a $Ar/CF_4/O_2$ mixture at 15 mTorr with and without the rf bias. The radially dependent IED for CF_3^+ is shown in Fig. 20(b). In both cases the IEDs are radially uniform in shape, but have peaks in the magnitude of the fluxes approximately at a third of the radius. The IEDs with the rf bias are shifted to higher energy by the amount of the dc bias (50–55 V) but are not dramatically altered since the sheath is essentially collisionless. The IED of Ar^+ is degraded somewhat in energy compared to the CF_3^+ since the former ion undergoes charge exchange collisions (both symmetric and identity changing) while the latter ions undergo largely elastic collisions. The symmetric charge exchange in Ar^+ results in an appreciable hot Ar atom flux to

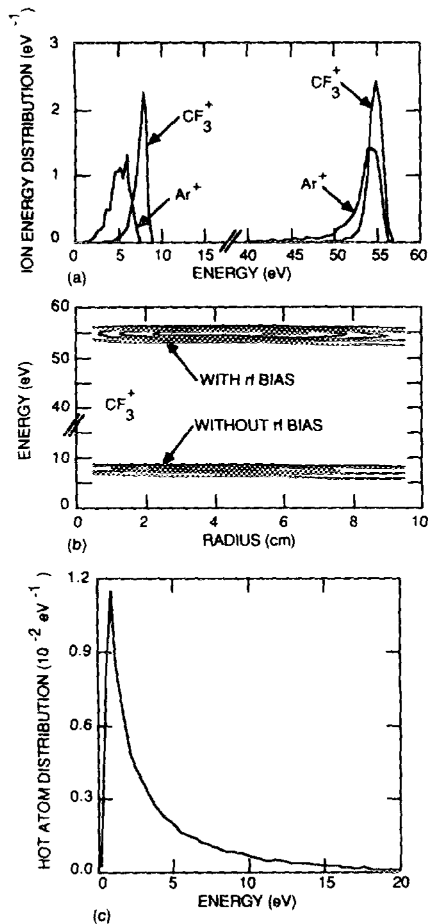

FIG. 20. Ion and hot atom distributions incident onto the substrate in ICP discharges sustained in $Ar/CF_4/O_2$ at 15 mTorr. Results are shown with and without a rf bias. (a) Ar^+ and CF_3^+ energy distributions averaged over the substrate; (b) CF_3^+ energy distribution as a function of radius; and (c) hot Ar atom distribution resulting from both symmetric charge exchange and reflection neutrals.

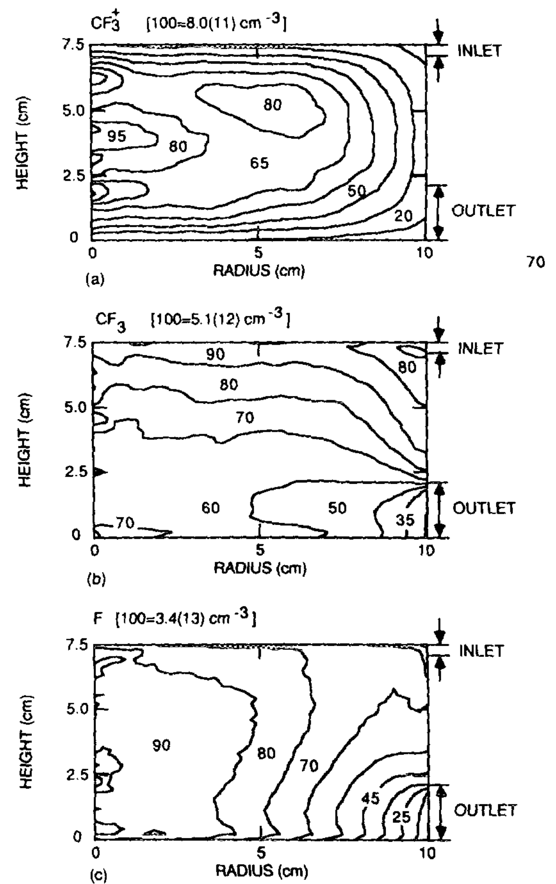

FIG. 21. Ion and radical densities obtained from the PCMCS as a function of position in an $Ar/CF_4/O_2$ discharge; (a) CF_3^+, (b) CF_3, and (c) F. The gas inlet (200 sccm) and outlet are shown. Ion pumping by CF_3^+ to the walls produces a large source of CF_3 at the surfaces. (See Fig. 5 for contour labeling scheme.)

the substrate, as shown in Fig. 20(c). Reflection neutrals (from ion impact) from the substrate and other surfaces also contributes to the hot atom flux.

The width of the IEDs of the ions undergoing only elastic collisions represent the range of plasma potentials at which the ions were formed, broadened somewhat by momentum transfer during the elastic collisions with neutrals having comparable masses. The widths of the IEDs do not dramatically change when applying the rf bias, a result which may be an artifact of the model. In the PCMCS we use time averaged electrostatic fields under the assumption that heavy ions will average the rf oscillations in the plasma potential by traversing the sheath over many rf cycles. In high plasma density sources, the sheath may be thin enough that the ion can traverse it in a single period. This would result in a somewhat bimodal broadening of the IED, as observed in low frequency, low plasma density RIE discharges.

The spatial distributions of CF_3^+, CF_3, and F, as calculated with the PCMCS, are shown in Fig. 21 without the rf bias. The locations of the gas inlet (height =0.25 cm) and outlet (height =2.0 cm) are noted. The total gas flow rate is 200 sccm. The CF_3^+ is formed by electron impact dissociation of CF_4 and by dissociative charge transfer from Ar^+ to CF_4 in approximately equal proportions. Its density has a diffusion dominated profile with an off-axis maximum mirroring its toroidal source function. The CF_3 density, shown in Fig. 21(b), is reduced near the inlet where the locally high inlet gas stream "blows" the CF_3 away from the inlet.

The reactive sticking coefficient for CF_3 used in the simulation is 0.02.[38] Since the fractional area of the outlet is larger than the reactive sticking coefficient, the largest sink for CF_3 is flow out the pump port, and not by reacting on the walls. This results in a significant decrease in the density of CF_3 leading toward the outlet. Similar trends are observed for F atoms, which has a somewhat higher reactive sticking coefficient in the model (0.04).

An important difference in the distributions of CF_3 and F results from the fact that in our reaction scheme we have CF_3^+ ions but not F^+ ions. The flux of CF_3^+ to the walls is large compared to the volumetric source of CF_3 radicals by electron impact dissociation of CF_4 and dissociative excitation transfer from Ar(4*s*). The CF_3^+ is neutralized at the walls and returns to the plasma as CF_3. This large source at the walls results in the density of CF_3 being maximum at the upper dielectric where the flux of CF_3^+ is the largest. Ion

pumping accounts for a large amount of recirculation of CF_3 radicals. This ion pumping process has been observed in ECR discharges where the flux of Ar^+ ions to the substrate exceeds the net gas flow through the discharge.[39] F atoms, without a source at the walls has its maximum density in the center of the plasma.

IV. CONCLUDING REMARKS

A 2D hybrid model has been developed for ICP reactors which includes the effects of capacitive coupling from the coils and from the rf applied to the reactor base. Plasma densities in excess of $10^{11}-10^{12}$ cm^{-3} have been found to result from rf powers of 500 W to 1 kW in rare gases or Penning mixtures. The inductive power is deposited toroidally within a skin depth below the dielectric roof and capacitively coupled power is deposited in the sheaths around the reactor walls. As a consequence of the toroidal inductive power deposition, the peak plasma densities in molecular gas mixtures are often off axis. Negative ion densities in low pressure, high plasma density plasmas are much less populous than in higher pressure parallel-plate plasmas. Since negative ions are believed to be precursors to dust particles, lower pressure high density plasmas may generate fewer particles.

ICP discharges with rf biases on the substrate resemble "externally" sustained discharges. The rf bias efficiently heats the tail of the electron distribution by stochastic processes, resulting in a significant increase in the total ionization and excitation rate which a moderate increase in power deposition. The effects of capacitive coil coupling are somewhat diminished by voltage dropped across the insulator. The capacitive coil coupling manifests itself by modulating the peak plasma potential and causing radially nonuniform structures in the plasma potential. These structures are more severe at low power deposition where the radially varying contact potential is less shielded.

The ion energy fluxes to the substrate in ICPs at 15 mTorr are fairly uniform as a function of radius. Ar^+ impinging on the substrate display energy distributions which are lower than CF_3^+ in $Ar/O_2/CF_4$ plasmas due to symmetric charge exchange with the Ar fill gas. An appreciable "hot" Ar atom population results.

ACKNOWLEDGMENTS

The authors would like to thank M. Barnes, J. Keller, J. O'Neill, T. Wicker, J. Cook, M. Turner, and A. Wendt for discussions on ICPs; and H. Pak and H. Riley for discussions on acceleration techniques. The authors would like to also thank J. Barrich for technical assistance. This work was supported by IBM East Fishkill Facility, LAM Research Corp., Sandia National Laboratory, Semiconductor Research Corp., and the National Science Foundation (ECS91-09362 and CTS91-13215). J. Barrich's assistance was supported by the NSF Research Experiences for Undergraduates Program.

[1] J. Asmussen, J. Vac. Sci. Technol. A **7**, 883 (1989).
[2] J. Hopwood, Plasma Sources Sci. Technol. **1**, 109 (1992).
[3] A. J. Perry, D. Vender, and R. W. Boswell, J. Vac. Sci. Technol. B **9**, 310 (1991).
[4] O. A. Popov, J. Vac. Sci. Technol. A **9**, 711 (1989).
[5] N. Sato, S. Iizuka, Y. Nakagawa, and T. Tsukada, Appl. Phys. Lett. **62**, 1469 (1993).
[6] T. J. Castagna, J. L. Shohet, D. D. Denton, and N. Hershkowitz, Appl. Phys. Lett. **60**, 2856 (1992).
[7] J. L. Cecchi, in *Handbook of Plasma Processing Technology*, edited by S. M. Rossnagel, J. J. Cuomo, and W. D. Westwood (Noyes, Park Ridge, NJ, 1990), Chap. 2.
[8] J. Keller, M. S. Barnes, and J. C. Forster, 42th Gaseous Electronics Conference, Urbana, Illinois, 1990 (unpublished), paper NA-5.
[9] J. H. Keller, J. C. Forster, and M. S. Barnes, J. Vac. Sci. Technol. A **11**, 2487 (1993).
[10] M. S. Barnes, J. C. Forster, and J. H. Keller, Appl. Phys. Lett. **62**, 2622 (1993).
[11] J. A. O'Neill, M. S. Barnes, and J. H. Keller, J. Appl. Phys. **73**, 1621 (1993).
[12] J. Hopwood, C. R. Guarnieri, S. J. Whitehair, and J. J. Cuomo, J. Vac. Sci. Technol. A **11**, 147 (1993).
[13] J. Hopwood, C. R. Guarnieri, S. J. Whitehair, and J. J. Cuomo, J. Vac. Sci. Technol. A **11**, 152 (1993).
[14] J. Hopwood, Appl. Phys. Lett. **62**, 940 (1993).
[15] A. E. Wendt, L. J. Mahoney, and J. L. Shohet, 45th Gaseous Electronics Conference, Boston, MA, 1992 (unpublished), paper LB-5.
[16] M. J. Kushner, T. J. Sommerer, and S. J. Choi, *Conference Record of the 1992 IEEE International Conference on Plasma Science* (IEEE, New York, 1992), p. 178.
[17] P. L. G. Ventzek, R. J. Hoekstra, T. J. Sommerer, and M. J. Kushner, Appl. Phys. Lett. **63**, 605 (1993).
[18] J-H. Tsai and C-H. Wu, J. Phys. D **26**, 496 (1993).
[19] M. Dalvie, M. Surendra, and G. S. Selwyn, Appl. Phys. Lett. **62**, 3207 (1993).
[20] D. P. Lymberopoulos and D. Economou, Appl. Phys. Lett. **63**, 2478 (1993).
[21] H. Pak and M. Riley, 45th Gaseous Electronics Conference, Boston, MA, 1992 (unpublished), paper BB-5.
[22] B. W. Yu and S. L. Girschick, J. Appl. Phys. **69**, 656 (1991).
[23] T. J. Sommerer and M. J. Kushner, J. Appl. Phys. **71**, 1654 (1992).
[24] Y. Weng and M. J. Kushner, Phys. Rev. A **42**, 6192 (1990).
[25] H. Hwang, R. Hui, K. James, and M. J. Kushner, J. Appl. Phys. **69**, 7419 (1991).
[26] M. S. Barnes, T. J. Colter, and M. E. Elta, J. Appl. Phys. **61**, 81 (1987).
[27] D. Lymberopoulos and D. Economou, J. Appl. Phys. **73**, 2668 (1993).
[28] M. Barnes (private communications, 1993).
[29] M. Hartig and M. J. Kushner, Appl. Phys. Lett. **62**, 1594 (1993).
[30] R. B. Piejak, V. A. Godyak, and B. M. Alexandrovich, Plasma Sources Sci. Technol. **1**, 179 (1992).
[31] M. Turner, Appl. Phys. Lett. (in press).
[32] T. J. Sommerer, H. Pak, and M. J. Kushner, J. Appl. Phys. **72**, 3374 (1992).
[33] A. V. Phelps, J. Res. Natl. Inst. Stand. Tech. **95**, 407 (1990).
[34] J. Hopwood, K. K. Reinhard, and J. Asmussen, J. Vac. Sci. Technol. A **8**, 3103 (1990).
[35] C. Lee, D. Graves, M. Lieberman, and D. Hess, J. Electrochem. Soc. (in press).
[36] A video animation of the plasma potential (r,z,t) is available from the authors. Enclose a standard VHS cassette with your request.
[37] W. L. Nighan, IEEE J. Quantum. Electron. **QE-14**, 714 (1978).
[38] Y. Hikosaka, H. Toyoda, and H. Sugai, Jpn. J. Appl. Phys. **32**, L690 (1993), and references cited therein.
[39] J. Forster and W. Holber, J. Vac. Sci. Technol. A **7**, 899 (1989).